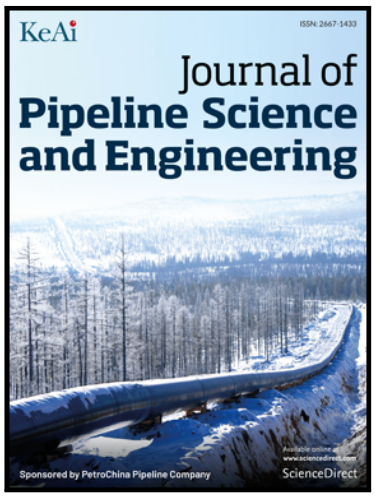

High Energy X-Ray Diffraction and Small-Angle Scattering Measurements of Hydrogen Fatigue Damage in AISI 4130 Steel

M.J. Connolly , J.S. Park , J. Almer , M.L. Martin , R. Amaro , P.E. Bradley , D. Lauria , A.J. Slifka

PII: S2667-1433(22)00040-3
DOI: https://doi.org/10.1016/j.jpse.2022.100068
Reference: JPSE 100068

To appear in: *Journal of Pipeline Science and Engineering*

Received date: 16 May 2022
Revised date: 3 June 2022
Accepted date: 4 June 2022

Please cite this article as: M.J. Connolly , J.S. Park , J. Almer , M.L. Martin , R. Amaro , P.E. Bradley , D. Lauria , A.J. Slifka , High Energy X-Ray Diffraction and Small-Angle Scattering Measurements of Hydrogen Fatigue Damage in AISI 4130 Steel, *Journal of Pipeline Science and Engineering* (2022), doi: https://doi.org/10.1016/j.jpse.2022.100068

High Energy X-Ray Diffraction and Small-Angle Scattering Measurements of Hydrogen Fatigue Damage in AISI 4130 Steel

M.J. Connolly[1], J.S. Park[2], J. Almer[2], M.L. Martin[1], R. Amaro[3], P.E. Bradley[1], D. Lauria[1], A.J. Slifka[1]

[1] *National Institute of Standards and Technology,325 Broadway, Boulder CO 80305*

[2] *Argonne National Laboratory, Lemont, IL, 604393*

[3] *Advanced Materials Testing Technology (AMTT), Pell City, AL 35128*

[*]Corresponding Author, matthew.connolly@nist.gov

ABSTRACT: Accurate lifetime predictions are critical for repurposing existing pipelines for hydrogen transmission as well as for developing novel steels which are minimally susceptible to lifetime degradation by hydrogen. Ultimately, lifetime prediction models assess the amount of damage a material undergoes during a typical service cycle and the cumulative damage a material can withstand prior to failure. However, not all damage processes are equal, and neither is the manner in which mechanical loading translates to damage the same when materials are in inert environments compared to in hydrogen environments. For example, in the three leading proposed mechanisms of hydrogen embrittlement (Hydrogen-Enhanced Decohesion (HEDE), the Hydrogen-Enhanced Localized Plasticity (HELP), and the Nano-Void Coalescence(NVC)), hydrogen is proposed to enhance the manifestation of grain separation, dislocation generation/movement, and void coalescence, respectively. A full understanding of the damage modes requires a measurement capable of probing all three mechanisms at once. Here we present simultaneous High Energy X-ray Diffraction (HEXRD) and Small-Angle X-ray Scattering (SAXS) during fatiguing of steel in hydrogen. HEXRD measurements probe strain and dislocation density; SAXS measurements probe nano-pore generation and coalescence. We will discuss the differences in damage modes between steels fatigued in air and in hydrogen and the role these difference play in lifetime predictions.

1. INTRODUCTION

As the global economy moves toward hydrogen as a fuel carrier [1], significant advancements are necessary to provide safe transport and storage options. The future of a hydrogen economy will rely on pipelines for hydrogen service [2]. This will include pipelines constructed of novel, hydrogen-resistant materials, as well as the re-purposing of existing pipelines which are constructed primarily of ferritic steel. Although some technological advances have come hand-in-hand with these economic forces, critical challenges still exist. In particular, hydrogen embrittlement (HE) of the structural materials needed to store and transport hydrogen is a severe hurdle for widespread use of hydrogen as an alternative fuel source [3]. Because of the hydrogen embrittlement effect, qualifying materials for hydrogen service requires extremely costly and time-consuming tests of mechanical performance in moderate- to high-pressure hydrogen. Although embrittlement can be easily observed in relatively fast and inexpensive quasi-static mechanical tests, the primary failure mode for pipelines is fatigue [4-6]. Therefore,

qualifying steels requires a statistically significant number of *cyclic* tests at moderate cycling frequencies, and full fatigue crack growth rate tests can each require several months to complete. A full set of data needed to qualify a single material can therefore require several months to years of measurements. Complete understanding of the mechanisms of hydrogen embrittlement and hydrogen assisted fatigue crack growth could allow for the development of a fatigue lifetime model which would significantly reduce the need for these long tests [7]. In turn, a complete understanding of the physical mechanisms underlying the embrittlement process is therefore necessary for cost-effective use of pipelines for hydrogen service.

Models for fatigue lifetime predictions utilize fatigue data and simulations to predict the total damage accumulated within a material per cycle, and the total accumulated damage a material can withstand prior to fracture [8]. During fully-reversed strain-life tests, for example, a set total strain is cyclically imposed onto a material until the material fails. A full strain-life data set (number of cycles to failure vs. applied strain amplitude) is therefore a powerful tool in predicting the fatigue lifetime of, for example, a pipeline. However, the strain-life of a material is drastically affected by the presence of hydrogen, where pipeline steels have been observed to fail after one to two orders of magnitude fewer cycles for the same strain amplitude compared to in air [9]. Because the same total strain is applied yet the material fails in fewer cycles, there are only two options: hydrogen affects the physical manifestation of plastic damage, or hydrogen affects the amount of plastic damage the material can withstand.

In one sense, the different proposed physical mechanisms for hydrogen embrittlement and hydrogen assisted fatigue can essentially be boiled down to differing on the proposed role of hydrogen on the type of plastic deformation undergone during straining. In the Hydrogen Enhanced Localized Plasticity (HELP) mechanism, for example, hydrogen is proposed to affect how plastic deformation manifests in the form of dislocation motion, through hydrogen-assisted enhancement in the dislocation mobility as well as an increase in dislocation density. In the intergranular Hydrogen Enhanced DEcohesion (HEDE) mechanism, hydrogen decreases the interaction strength between neighboring grains, and plastic strain manifests as inter-granular separation. In the Nanovoid Coalescence (NVC) mechanism, hydrogen stabilizes plastic damage via nanovoid formation leading to void coalescence [10,11]. Discerning between the different proposed mechanisms therefore ultimately comes down to determining how hydrogen affects the mode of plastic damage a material undergoes during straining, and how hydrogen affects the amount of plastic damage the material can withstand prior to failure.

Some researchers have suggested a "synergistic interplay" of hydrogen embrittlement process [12,13]. It is therefore necessary to measure, simultaneously, multiple mechanisms of damage. Combined high-energy Wide-Angle X-ray Scattering (WAXS) and Small-Angle X-ray Scattering (SAXS) has the ability to measure each of the aforementioned forms of plastic damage. WAXS has been shown to be a powerful tool for measuring both the elastic strain and dislocation density near fatigue cracks grown in steel exposed to hydrogen [14,15]. SAXS probes larger structures compared to WAXS, and is sensitive to differences in scattering length density (e.g. differences in bulk metal and void space). SAXS has been used to measured nanoscale voids arising from plastic deformation in steel, brass, and aluminum [16-18]. Importantly, the 1-ID beamline at Argonne National Laboratory's Advanced Photon Source (APS) has a detector arrangement which allows for simultaneous WAXS and SAXS measurements. Therefore, one can perform simultaneous mappings of strain, dislocation density, and nanovoid density ahead of crack tips.

In this work we have performed a strain and dislocation density mapping with the intent to better understand the interplay between the HEDE and HELP mechanisms acting during strain-life testing in a 4130 steel. Additionally, the nanovoid structure was mapped through SAXS to determine the role of the NVC mechanism.

2. MATERIAL AND SAMPLE PREPARATION DETAILS

AISI 4130 steel is a quenched and tempered steel with a ferrite/martensite microstructure and has a 0.2% offset yield strength of 604 ± 7 MPa, an ultimate tensile strength of 780 ± 8 MPa, and a Young's modulus of 200 ± 14 GPa. In air, the elongation to failure is 41.9 ± 1%. The chemical composition of the steel is listed in Table 1.

Table 1: Chemical composition (in mass %) of the AISI 4130 steel used in this study.

Element	Fe	Cr	Mn	C	Si	Mo	S	P

Mass %	97.749	1.03	0.5	0.32	0.21	0.17	0.01	0.011

The samples were machined into round specimens with button-head style grips and gage section diameter of 6.35 mm (0.250''). Two samples were mechanically actuated, one in air and one in hydrogen, in a fully-reversed ($R = \varepsilon_{min}/\varepsilon_{max}$ = -1) strain-life measurement according to ASTM E606 with a strain amplitude ε_a = 0.02. All samples were mechanically actuated at room temperature. A third sample was characterized by SAXS and WAXS in the as-machined condition. For the sample prepared in hydrogen, the gas pressure was 18 MPa (2600 psi). Prior to loading hydrogen at the set pressure, the pressure chamber was first purged with 14 MPa (2000 psi) of hydrogen for one purging cycle, followed by three purging cycles using 14 MPa hydrogen. Mechanical actuation was stopped after a crack had initiated but prior to a complete separation of the sample. The initiation of a crack in each sample was indicated by a drop in the maximum force during cycling. The inset in Figure 1 shows each sample's position along the strain-life curves in air and in hydrogen. The sample cycled in air had a crack form after 206 strain reversals, while the sample cycled in hydrogen had a crack form after 22 strain reversals. Figure 1 illustrates the stabilized cycle for both samples, and the contribution of plastic strain (ε_{pl}) and elastic strain (ε_{el}) to the total strain [19]. The total strain was dominated by plastic strain for both samples, however the sample cycled in hydrogen had a larger plastic strain contribution and smaller elastic strain contribution compared to the sample cycled in air.

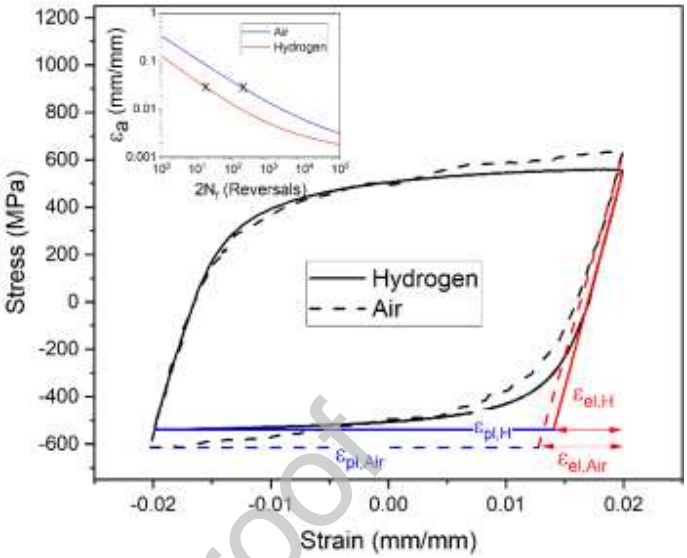

Figure 1: Stabilized cycle for fully-reversed (R = -1) strain-life tests in air and in hydrogen with a strain amplitude of 0.02. The strain-life in hydrogen was an order of magnitude lower than in air (see inset), and the elastic and plastic strain contributions differed between the specimens cycled in the two environments.

3. EXPERIMENTAL DETAILS

The samples were transported to Argonne National Laboratories (ANL) Advanced Photon Source (APS) 1-ID-E end station for WAXS and SAXS measurements. The layout of the APS 1-ID-E end station is shown in Figure 2. Crack tip strain and dislocation density mapping were performed in a manner similar to our earlier work, outlined in Ref. 11. In addition to WAXS, SAXS signal was captured using the SAXS / WAXS detector arrangement descripted in Refs. [18,19] to capture SAXS and WAXS signal concurrently. Figure 2 illustrates the measurement geometry. The WAXS detector array was positioned approximately 2.3 meters from the sample, and the SAXS detector was approximately 6 meters from the sample.

The measurements were performed using 80.73 keV x-rays. The beam was narrowed by a series of slits to a beam size of 120×120 μm^2. The samples were mounted on a stage capable of translations perpendicular to the beam in the horizontal and vertical directions. For the WAXS measurements, a pixelated area detector with 200 μm pixel pitch and 2048×2048 pixel array was used. A standard CeO_2 powder sample [22] was used for calibration of the WAXS detector distance and tilt. The SAXS detector had a 58 μm pixel pitch and a momentum transfer Q-range of 0.35 to 13 nm^{-1}. Calibration of the SAXS detector distance and tilt was performed using a silver behenate ($AgC_{22}H_{43}O_2$) sample. SAXS intensity from a glassy carbon standard [23] was used to calibrate the measured SAXS intensity and determine the absolute intensity. Simultaneous WAXS and SAXS scans were performed within the gage section of the specimens with step sizes of 0.29 mm along the long axis of the specimens. For each lateral step,

measurements were taken as the sample was rotated from -45° to +45° with a step size of 5°. The measurements taken at each rotation were used to determine inverse pole figures, while the strain, dislocation density, and SAXS intensity were determined from an average over the rotation angles. Pore size distributions were determined using a spherical pore model in the GSAS software package [24].

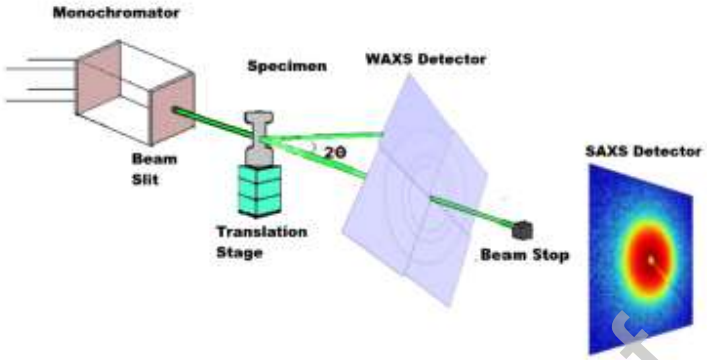

Figure 2: Experimental geometry and coordinate system. The samples were aligned such that the long axis of the sample was vertical. The samples were rotated about their long axis for pole figure measurements.

4. RESULTS

Figure 3 (center) shows the strain and dislocation density mapped along the gauge section for the reference sample and samples cycled in air and in hydrogen. The strain in the reference sample is consistent, and near-zero, throughout the entirety of the gauge section, which indicates that the as-machined sample does not contain significant residual stresses. Similarly, the dislocation density in the reference sample is essentially constant and has a value of approximately $2x10^7$ m^{-2}. The strain in the sample cycled in hydrogen is tensile in the center of the sample and decreases close to zero moving away from the center except in two areas with sharp increases in strain. These sharp increases in strain are indicative of cracks which formed as the samples failed. Near the left crack (Crack A), there is an increase in dislocation density by approximately two orders of magnitude over the dislocation density in the reference sample, and approximately 1.5 orders of magnitude over the dislocation density in the center of the sample. The dislocation density is also increased near the right crack (Crack B), however in the immediate vicinity of the crack a notable drop in dislocation density was observed. The x-ray transmission through the sample was larger near crack A compared to near crack B, indicating that crack B had not grown to the same extent as crack A, and was closer to initiation. Crack B's growth was likely halted by the propagation of Crack A

The sample cycled in air has near-zero strains near the edges of the gauge section and compressive strains toward the center. The difference in direction of the strains between the sample cycled in air and the sample cycled in hydrogen is likely due to whether the cycling was stopped during the tensile or compressive portion of the cycling. A sharp area of compressive strain is observed in the center of the sample cycled in air. As in the sample cycled in hydrogen this is indicative of a crack. An increase in dislocation density is also observed near the crack in the sample cycled in air. The magnitude of the increased dislocation density is smaller than that of crack A and slightly higher than that of crack B in the sample cycled in hydrogen.

A representative loading-axis {001} inverse pole figure for the reference sample is shown on the top right of Figure 3. The reference sample shows some texture with bright red spots near {111} and {012} and blue near {001}, indicating a larger number of grains were oriented with their crystal {111} and {012} axes along the loading axis, and a dearth of grains oriented with crystal {001} axis along the loading axis. The texture of the sample cycled in hydrogen is largely unchanged compared to the reference sample. At the center of the specimen, where the strain is increased but a crack has not formed, the texture loses some intensity near {012}. The texture near crack B is slightly stronger than near crack A. Compared to the reference sample, the sample cycled in air loses nearly all texture, both near and away from the crack.

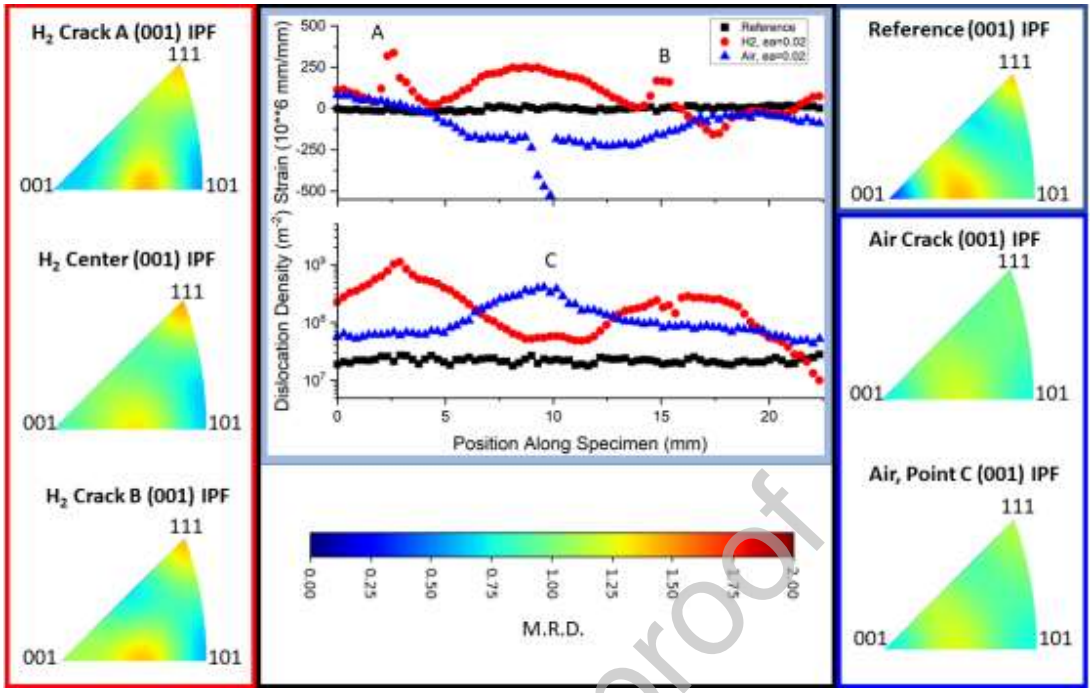

Figure 3: Left: (001) Inverse pole figures (IPF) for the sample strained in hydrogen, at the center of the sample and near Crack A and Crack B. The color in each IPF indicates the multiples of random distribution (M.R.D.) as in the scale bar at the figure bottom. Center: Loading-axis strain and dislocation densities for the reference sample (black) and failed samples cycled in hydrogen (red) and in air (blue). Right: (001) IPF for the reference sample measured at the center of the sample and for the failed samples near the crack and near the position labeled "C" in the sample strained in air.

A representative SAXS curve from the reference sample, at cracks A and B of the sample strained in hydrogen, and near the crack in the sample strained in air are shown in Figure 4. SAXS intensity arises from a contrast between scattering length densities of the components in the sample. In this case, the contrast is between the metallic lattice and pores in the sample. The size of the probed pores is inversely proportional to the momentum transfer *Q*. The *Q*-range in this experiment probes pores roughly of diameter 2-50 nm.

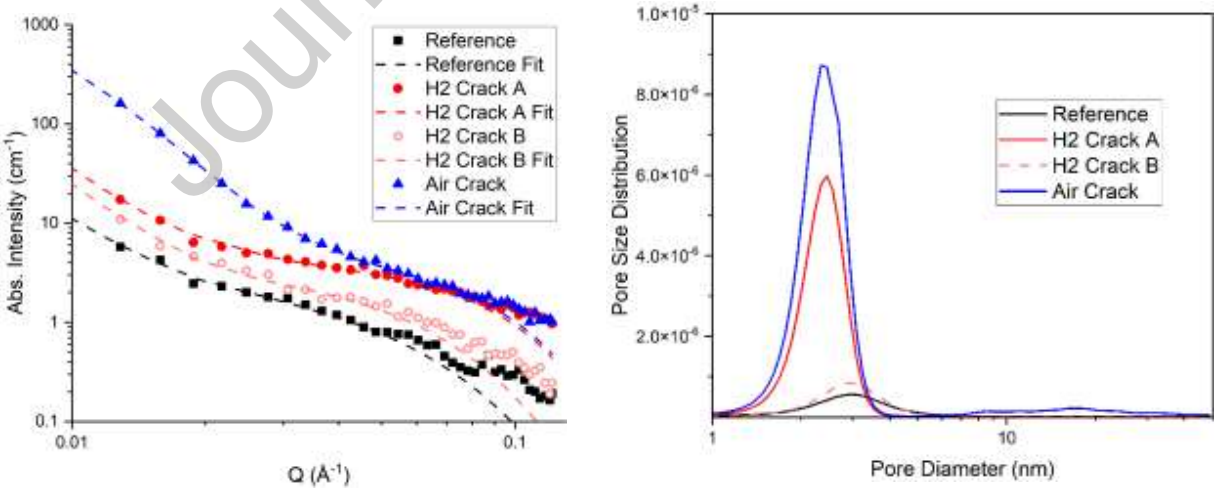

(a) (b)

Figure 4: (a) SAXS curves from the center of the reference specimen (black), hydrogen Crack A (red), hydrogen Crack B (light red), and air Crack (blue). The dashed lines are fits to a spherical pore model, which correspond to the pore size distributions in (b).

The reference sample exhibits relatively weak SAXS intensity, indicating a small volume of pores in the unstrained sample. The SAXS intensity increases slightly near crack B in the sample cycled in hydrogen, but the general Q-dependence was not changed compared to the reference sample. In contrast, near crack A the high-Q SAXS intensity is increased compared to the reference sample, indicating an increase in the volume of smaller pores compared to the reference sample. Crack A shows similar SAXS intensity in the low-Q region as the reference sample. The high-Q SAXS intensity from crack A overlaps that of that from the crack in the specimen strained in air, however the low-Q SAXS intensity is much larger in the air sample, which indicates an increase in larger pores. Figure 4 shows the pore size distribution from fitting the SAXS curves to a spherical pore model. Both the air crack and the hydrogen crack A show peaks in the pore size distribution at around 2.5 nm. The air crack has developed some pores at around 20 nm.

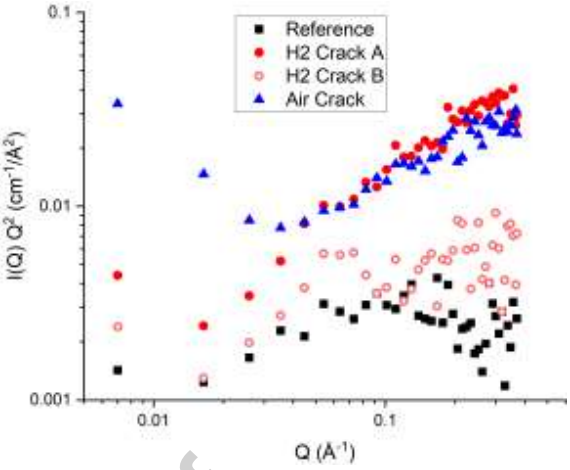

Figure 5: The Kratky plot (I Q²) for the reference and crack B in the hydrogen sample bend over at high-Q, indicating a disconnected network of voids, while crack A and the crack in the air sample diverge at high-Q, indicating a structure.

The Kratky plot (IQ^2 vs. Q), where *I* is the SAXS intensity, provides information about the configuration of pores in the material. Kratky plots accentuate differences in the scattering at high-*Q*. Kratky plots which bend over at high-Q, as in the Reference sample, indicate an array of disconnected pores. On the other hand, Kratky plots which increase at high-Q indicates an extended network of larger pores connected by smaller pores. Such increase is observed for crack A in the sample strain in hydrogen and in the crack in the sample strained in air. Therefore, the Kratky plots suggest nanovoids have begun coalescing near the crack in the sample cycled in air and crack A in the sample cycled in hydrogen. The plateau at high-Q in the Kratky plot from the SAXS measured near crack B in the sample cycled in hydrogen may indicate a partially connected network of pores that have not coalesced to the same extent as near crack A and the air crack.

5. DISCUSSION

When the 4130 steel is cyclically strained in air, the material failed after 206 strain reversals; when cyclically strained in hydrogen, failure occurs after only 22 strain reversals. This order-of-magnitude decrease in strain-lifetime indicates hydrogen either decreases the ability of the material to withstand plastic deformation prior to fracture or changes the mode of plastic deformation undergone when strained. The WAXS and SAXS results shown here probe three different mechanisms of plastic deformation: generation of dislocations, rotation of grains, and formation of pores.

Large strain intensities were observed near the cracks formed as the 4130 steel failed, both in air and in hydrogen. Near these cracks, the dislocation density is increased compared to the background. The dislocation density is larger near crack A of the sample fatigued in hydrogen compared to near the crack of the sample fatigued in air (~$2*10^9$ m^{-2} compared to ~$5*10^8$ m^{-2}). This increase in dislocation density in hydrogen is consistent with – and may be a consequence of – the HELP mechanism which predicts a decrease in dislocation interaction leading to an increase in dislocation density. However, the differences in magnitude are not large. Interestingly, the sample grown in hydrogen shows a very local decrease in dislocation density near crack B. We have previously reported the strain and dislocation density ahead of AISI 4130 steel crack tips grown in air and in hydrogen [11], which showed a decrease in dislocation density approximately 2 mm ahead of the crack tip. The fracture surfaces after the fatigue crack growth rate (FCGR) test indicated an increase in intergranular fracture in hydrogen. Coupled with the promotion of intergranular fracture, the effect of hydrogen on the dislocation density suggested a mechanism of hydrogen-assisted fatigue in which hydrogen enhances dislocation pileup at grain boundaries, promoting plastic

deformation by intergranular fracture. However, this drop was only observed in the smaller of the two cracks, crack B. Because crack B was closer to the initiation stage compared to crack A, one explanation is that the dislocation pileup at grain boundaries occurs prior to fracture, and further cycling redistributes the dislocation density through the grains. However, further characterization will be necessary to confirm this.

Inverse pole figures show that the texture of the sample fatigued in hydrogen is relatively unchanged during straining compared to the reference unstrained sample, both near and far from the cracks. Conversely, the grains in the air sample are shown to move from a measurable crystallographic texture to an untextured, nearly perfectly random set of grain orientations. This suggests that one role of hydrogen may be to "lock" the grains into their initial orientation. While in air the strain energy can go into plastic deformation which results in reorientation of grains, the strain energy imparted on the sample in hydrogen must go into plastic deformation with different results to the microstructure.

The SAXS curves show the formation of nanopores in both strained samples. The Kratky plots indicate the pore structure moves from an unconnected distribution of pores in the reference sample to a connected, coalesced type structure. The pore size distributions indicate that the connected structure in hydrogen is comprised only of small nanopores (~2.5 nm), while the structure for the sample in air has some larger pores (~20 nm). The proposed NVC mechanism is predicated on the argument that hydrogen stabilizes nanovoids which promotes their coalescence into larger voids. However, the results here suggest nanovoid stabilization is not unique to steels strained in hydrogen since nanovoids were observed in both air and hydrogen. The lack of larger nanovoids near the cracks in the sample cycled in hydrogen suggests that fracture occurred in the sample strained in hydrogen before these nanovoids could coalesce into the larger pores.

6. CONCLUSIONS

Here we have presented strain, inverse pole figures, dislocation density, and void structure in a AISI 4130 steel subjected to fully-reversed fatigue cycling for samples tested in air and in hydrogen. Sharp increases in strain were observed near the fatigue cracks. The inverse pole figures indicate a lower degree of grain rotation during cycling for the sample tested in hydrogen compared to in air. Dislocation density was observed to increase near the fatigue cracks, with a slightly higher density near the main crack grown in hydrogen. A drop in dislocation density was observed near a secondary crack in the sample grown in hydrogen, possibly indicating dislocation build up at grain boundaries prior to fracture. SAXS curves show differences in the size and morphology of the nanovoid between the sample cycled in hydrogen and the sample cycled in air. The results presented here certainly indicate that multiple modes of deformation are acting during straining in hydrogen. Ultimately the power of the combined WAXS and SAXS measurements is the ability to probe multiple deformation modes at once. Further measurements, as well as modeling of the energetics of these deformation modes, will provide a pathway for accurate for lifetime predictions of the materials which comprise current and future pipelines.

Declaration of interests

☒ The authors declare that they have no known competing financial interests or personal relationships that could have appeared to influence the work reported in this paper.

7. Acknowledgements

This research used resources of the Advanced Photon Source, a U.S. Department of Energy (DOE) Office of Science user facility at Argonne National Laboratory and is based on research supported by the U.S. DOE Office of Science-Basic Energy Sciences, under Contract No. DE-AC02-06CH11357.

8. REFERENCES

[1] Obama, B. (2017). "The Irreversible Momentum of Clean Energy", *Science*, AAAS, Volume 355, No. 6321, pp. 126-129.

[2] Martin, M., Connolly, M., DelRio, F. and Slifka, A. (2020). "Hydrogen embrittlement in ferritic steels", *Applied Physics Reviews*, Volume 7, No. 4, pp. 041301.

[3] "Hydrogen Pipelines" (2021), *Energy.gov*, https://www.energy.gov/eere/fuelcells/hydrogen-pipelines.

[4] Walter, R. and Chandler, W. T. (1973), "Influence of gaseous hydrogen on metal", *Final Report No. NASA-CR-124410*.

[5] Amaro, R. L., White, R. M., Looney, C. P., Drexler, E. S., and Slifka, A. J. (2018). "Development of a Model for Hydrogen-Assisted Fatigue Crack Growth of Pipeline Steel." *ASME. J. Pressure Vessel Technol.*, Volume 140, No. 2, pp. 021403.

[6] San Marchi, C. and Somerday, B. P. (2012), "Technical reference on hydrogen compatibility of materials: Plain carbon ferritic steels: C-Mn alloys (code 1100)," *Sandia Report*, No. SAND2012-7321, see http://www.sandia.gov/matlsTechRef/.

[7] Looney, C., Hagan, Z., Connolly, M., Bradley, P., Slifka, A., and Amaro, R. (2020). "Modelling the test methods used to determine material compatibility for hydrogen pressure vessel service", *International Journal of Fatigue*, Volume 132, pp. 105339.

[8] Neeraj, T., Srinivasan, R., and Li, J. (2012). "Hydrogen embrittlement of ferritic steels: observations on deformation microstructure, nanoscale dimples and failure by nanovoiding", *Acta Materialia*, Volume 60 No. 13-14, pp. 5160-5171.

[9] Martin, M. L., Looney, C., Bradley, P., Lauria, D., Amaro, R., & Slifka, A. J. (2019). Unification of hydrogen-enhanced damage understanding through strain-life experiments for modeling. *Engineering fracture mechanics*, Volume 216, pp. 106504.

[10] Nagumo, M., Nakamura, M., & Takai, K. (2001). "Hydrogen thermal desorption relevant to delayed-fracture susceptibility of high-strength steels", *Metallurgical and Materials Transactions A*, Volume *32*, No. 2, pp. 339-347.

[11] Takai, K., Shoda, H., Suzuki, H., and Nagumo, M. (2008). "Lattice defects dominating hydrogen-related failure of metals" *Acta Materialia*, Volume *56*, No. 18, pp. 5158-5167.

[12] Djukic, M. B., Bakic, G. M., Zeravcic, V. S., Sedmak, A., and Rajicic, B. (2019). "The synergistic action and interplay of hydrogen embrittlement mechanisms in steels and iron: Localized plasticity and decohesion", *Engineering Fracture Mechanics*, Volume *216*, pp.106528.

[13] Bouledroua, O., Hafsi, Z., Djukic, M. B., and Elaoud, S. (2020). "The synergistic effects of hydrogen embrittlement and transient gas flow conditions on integrity assessment of a precracked steel pipeline", *International Journal of Hydrogen Energy*, Volume *45*, No. 35, pp. 18010-18020.

[14] Connolly, M., Martin, M., Bradley, P., Lauria, D., Slifka, A., Amaro, R., and Park, J. S. (2019). "In situ high energy X-ray diffraction measurement of strain and dislocation density ahead of crack tips grown in hydrogen", *Acta Materialia*, Volume *180*, pp. 272-286

[15] Withers, P. J. (2015). "Fracture mechanics by three-dimensional crack-tip synchrotron X-ray microscopy", *Philosophical Transactions of the Royal Society A: Mathematical, Physical and Engineering Sciences*, Volume 373, No. 2036, pp. 20130157.

[16] Wang, L., Li, M., and Almer, J. (2013). "In situ characterization of Grade 92 steel during tensile deformation using concurrent high energy X-ray diffraction and small angle X-ray scattering", *Journal of nuclear materials*, Volume 440, No. 1-3, pp. 81-90

[17] Pan, X., Wu, X., Mo, K., Chen, X., Almer, J., Ilavsky, J., and Stubbins, J. F. (2010). "Lattice strain and damage evolution of 9–12% Cr ferritic/martensitic steel during in situ tensile test by X-ray diffraction and small angle scattering", *Journal of Nuclear Materials*, Volume *407*, No. 1, pp. 10-15.

[18] Chaudhuri, A., Singh, M. A., Diak, B. J., Cuoppolo, C., and Woll, A. R. (2013). "Nanovoid characterization of nominally pure aluminium using synchrotron small angle X-ray Scattering (SAXS) methods", *Philosophical Magazine*, Volume *93*, No. 35, pp. 4392-4411.

[19] Dowling, N. E. (1971). Fatigue failure predictions for complicated stress strain histories. Department of Theoretical and Applied Mechanics. College of Engineering. University of Illinois at Urbana-Champaign.

[20] Haeffner, D. R., Almer, J. D., & Lienert, U. (2005). The use of high energy X-rays from the Advanced Photon Source to study stresses in materials. *Materials Science and Engineering: A*, Volume *399, No.* 1-2, pp. 120-127.

[21] Park, J. S., Zhang, X., Sharma, H., Kenesei, P., Hoelzer, D., Li, M., & Almer, J. (2015). High-energy synchrotron x-ray techniques for studying irradiated materials. *Journal of Materials Research*, Volume *30, No.* 9, pp. 1380-1391.

[22] D. L. Kaiser and J. R. L. Watters, "National Institute of Standards & Technology Standard Reference Material674b X-Ray Powder Diffraction Intensity Set for Quantitative Analysis by X-Ray Powder Diffraction," (2007).

[23] Zhang, F., Ilavsky, J., Long, G. G., Quintana, J. P., Allen, A. J., & Jemian, P. R. (2010). Glassy carbon as an absolute intensity calibration standard for small-angle scattering. *Metallurgical and Materials Transactions A*, Volume *41,* No. 5, pp. 1151-1158.

[24] Toby, B. H., Von Dreele, R. B. (2013). "GSAS-II: the genesis of a modern open-source all purpose crystallography software package". *Journal of Applied Crystallography*, Volume 46, No. 2, pp. 544-549. doi:10.1107/S0021889813003531